Computers & Fluids 65 (2012) 56–65

Contents lists available at SciVerse ScienceDirect

Computers & Fluids

journal homepage: www.elsevier.com/locate/compfluid

Flow structures in cerebral aneurysms

A.M. Gambaruto *, A.J. João

Department of Mathematics and CEMAT/IST, Instituto Superior Técnico, Technical University of Lisbon, Av. Rovisco Pais 1, Lisbon 1049-001, Portugal

ARTICLE INFO

Article history:
Received 9 December 2011
Accepted 22 February 2012
Available online 9 March 2012

Keywords:
Description of flow field
Flow structures
Cerebral aneurysm
Computational haemodynamics
Critical points
Vortex core extraction

ABSTRACT

Mechanical properties of blood flow are commonly correlated to a wide range of cardiovascular diseases. In this work means to describe and characterise the flow field in the free-slip and no-slip domains are discussed in the context of cerebral aneurysms, reconstructed from in vivo medical imaging. The approaches rely on a Taylor series expansion of the velocity field to first order terms that leads to a system of ODEs, the solution to which locally describes the motion of the flow. On performing the expansion on the vessel wall using the wall shear stress, the critical points can be identified and the near-wall flow field parallel to the wall can be concisely described and visualised. Furthermore the near-wall expansion can be expressed in terms of relative motion, and the near-wall convective transport normal and parallel to the wall can be accurately derived on the no-slip domain. Together, these approaches give a viable and robust means to identify and describe fluid mechanic phenomena both qualitatively and quantitatively, leading to feasible practical use in biomedical applications.

From analysis of steady and unsteady flow simulations in two anatomically accurate cerebral saccular aneurysm cases, a set of measures can be readily obtained at all time intervals, including the impingement region, separation lines, convective transport near the wall and vortex core lines or structures, which have all been related to diseased states. Other fluid mechanic measures are also discussed in order to give further detail and insight during post-processing, and may play an important role in the growth and rupture of the aneurysm.

1. Introduction

It is commonly accepted that certain fluid mechanic measures in arterial haemodynamics are linked to disease formation such as atheroma and aneurysms, and play a role in vascular remodelling. While the relationship between the flow field and disease is not fully understood, fluid mechanics parameters on and near the artery wall, such as wall shear stress (WSS) and derived measures, residence times and region of flow impingement are among the most commonly sought correlators to disease. This is often discussed in relation to mechanotransduction and mass transport. In this work some physical insight of these parameters is presented and then related to possible signalling mechanisms that endothelial cells may be endowed with. In this work the flow structures for two patient-specific saccular cerebral aneurysm, shown in Fig. 1, are studied at steady-state and unsteady periodic simulations, identifying feasible means to describe and extract relevant flow measures.

The non-planarity and tortuousity of vessels play a determining role in the human arterial system, resulting in a strong influence of the local vessel topology on the flow field [1–6]. An abnormal flow field, usually described as complex and disturbed, is often related to the diseased states. Elevated WSS values have also been associated with aneurysm formation [7,8], while temporal and spatial gradients and temporal directional fluctuations [9–13] of WSS have also been studied in relation to aneurysm initiation and rupture. Vascular remodelling is thought partly as an adaptive response to alleviate undesired haemodynamic conditions, such as high WSS and spatial WSS gradients in aneurysm formation [8,11], or low and disturbed WSS in anastomosis remodelling and atherosclerosis [14,15]. Flow structures and their stability within the cardiac cycle have also been associated to aneurysm rupture [13,16]. Despite the consensus that the haemodynamic and mechanical properties in relation to aneurysms play a crucial role, there is still substantial debate as to the most appropriate measures to discuss patient healthcare and risks of rupture; furthermore the pathophysiology of cerebral aneurysms includes considerations of factors such as genetic predisposition and biochemical reactions [17–20].

Aneurysms are often studied from a geometrical standpoint, since in effect the shape of the aneurysm and the parent artery act as boundary conditions and will determine the flow field (as well as the fluid boundary conditions at artificial sections). Among these studies the curvature of the parent vessel upstream to the aneurysm has been correlated to aneurysm rupture [21] and often

* Corresponding author. Tel.: +351 218419638.
E-mail address: agambar@math.ist.utl.pt (A.M. Gambaruto).

0045-7930/$ - see front matter © 2012 Elsevier Ltd. All rights reserved.
http://dx.doi.org/10.1016/j.compfluid.2012.02.020

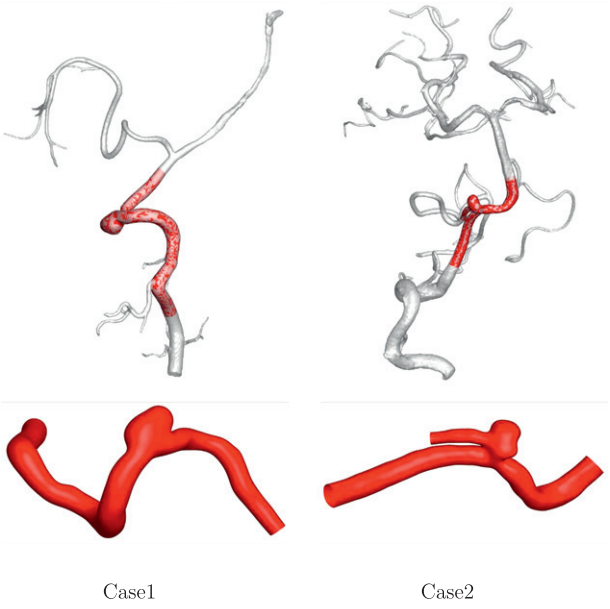

Fig. 1. Top row: region of segmented cerebral vasculature and region of interest containing the aneurysm (flow is from bottom to top) for two patient data sets. Bottom row: detail of region of interest used as computational domain (flow is from left to right).

the shape of the aneurysm is the most used criterion for clinical decisions [22,23].

In this work methods based on existing theory of critical points [24–26] are used to characterise concisely both the free-slip (fluid away from the wall) and no-slip (fluid on or near the wall) domains. These methods are shown to give a description of the flow field in a simple approach, both to implement and also as tools to analyse the data. These methods are meant to complement and assist the current trend of studies of diseases of human physiology related to haemodynamics.

The outline of the paper is as follows: a brief overview of the patient data sets and the approach of reconstructing a computational domain from medical images is given in Section 2. The parameters for the numerical simulations are detailed in Section 3. In Section 4 the outline of the theory on the Taylor series expansions of the velocity, the wall shear stress and the relative position is presented, and related to critical point theory. The results are presented in Section 5 and finally the conclusions are drawn in Section 6.

2. Patient data sets

In this work two patient-specific geometries were reconstructed from medical images obtained in vivo from rotational computed tomography angiography (CTA), provided as volumetric data with voxel resolution of $\sim$0.4 mm on a 512^3 grid. The reconstruction procedure of the 3D geometry surface for numerical simulations consists in image segmentation and surface extraction, followed by surface smoothing and identifying the region of interest, and finally meshing.

A constant threshold value for segmenting the image data is initially used, followed by a manual refinement to exclude the most significant noise and artefacts. The contrast of object to background using rotational CTA images is sufficiently large to allow this approach to be reliable. A marching tetrahedra algorithm, with linear interpolation of the greyscale, is used directly on the voxel data to extract the 3D surface to yield an initial triangulation. This is admissible due to the voxel fine resolution and uniform size. Together, the approach described so far is relatively fast and inexpensive, with little effective user intervention. Several other possibilities exist to reduce the user intervention and adopt more automatic techniques, and the most popular of these is use of deformable models [27,28], however each method has its limitations and at times necessitates corrective user intervention or careful coefficient choice. Ultimately there is a uncertainty in the segmented geometry that is limited by the acquisition modality, resolution, contrast and noise.

The resulting virtual model of the vasculature is then prepared for the numerical simulations by identifying the regions of interest and removing secondary branches that are located far from the aneurysm. Surface smoothing is then employed to reduce small surface perturbations due to medical imaging noise and resolution in combination with the segmentation approach. Smoothing is performed using the bi-Laplacian method, an iterative method which resembles an explicit time marching scheme, and a final small inflation along the local normal by a constant distance in order to minimise the volume alteration and surface distortion [29]. The intensity of the smoothing, hence the number of iterations performed, is chosen to reduce the surface curvature variation with the constraint that the resulting surface definition does not deviate from the original more than half the voxel size, which is the basic unit size of uncertainty in interpreting the medical images.

Fig. 1 shows the cerebral arterial geometry surfaces, with several secondary branches and the saccular aneurysms, as well as the resulting region of interest that includes the aneurysm and is used in the numerical simulations. In the models used as computational domain, any secondary branches far from the aneurysm were excluded and the parent artery is truncated with sections locally perpendicular to the axis of the vessel and in a region where the vessel is relatively straight. The secondary branches are removed to reduce computational cost, and since far from the aneurysm they have a reduced effect on the flow field in the sac, with the error incurred comparable to other modelling uncertainties [27]. Furthermore a long upstream section was chosen in order to reduce effects of inflow boundary condition choice on the resulting computed solution.

3. Parameters of the computational haemodynamics

The computations were performed using OpenFOAM software package [30] to solve the Navier–Stokes equations, which relies on the finite volume method. The simulations were run for steady-state for the two patient cases and unsteady for Case 1. These simulations were chosen in order to be able to both emphasise the use of the proposed methods clearly with steady-state, as well as demonstrate the relevance in more physiological scenario with the unsteady computations. The schemes used are the well known SIMPLE method for the steady-state and PISO for the unsteady computations. Convergence criterion was set to 10^{-8} on the residual.

The vessel wall was assumed rigid and the fluid boundary conditions were chosen to be no-slip for the vessel wall, a zero pressure gradient was prescribed at the outflows (including for the secondary vessel for Case 2) and the inflow flow rate was obtained using the relation $Q = k \cdot A^n$ (where $k = 48.21$ and $n = 1.84$) [31]. The cross-sectional areas of both cases was found to be almost identical, resulting in a $Q = 4 \times 10^{-6}\,\mathrm{m^3\,s^{-1}}$, hence $Re \approx 260$. The fluid is modelled as Newtonian and incompressible, and the kinematic viscosity was chosen to be $\nu = 3.883 \times 10^{-6}\,\mathrm{m^2\,s^{-1}}$ and the density $\rho = 1030\,\mathrm{kg/m^{-3}}$. The unsteady waveform was scaled from that provided in [13] and the time step was chosen to be 0.0085 s, hence 100 steps for each heartbeat (0.85 s), and a total of fifteen heartbeats were simulated to avoid transients due to the initial conditions (zero velocity and pressure).

The mesh consists in unstructured tetrahedral elements, created using the Gmsh software package [32]. Mesh convergence studies were carried out on Case 1, using a 0.8 M and 4.6 M element meshes for the steady-state computations, based on differences in the interpolated velocity field. The unsteady simulations were performed with the coarser mesh size. The mesh for Case 2 comprised of 2.6 M elements, since the length of the computational domain is less than for Case 1.

4. Methods for analysing the flow field

In this section methods for characterising the flow field are presented, based on truncated Taylor expansions of velocity, wall shear stress or relative position. The free-slip and no-slip regions of the flow field are considered individually. The free-slip domain description of the fluid mechanics is based on the velocity gradient tensor, while for the no-slip region the wall shear stress gradient tensor is used and finally the local convective transport and momentum transfer is described in terms of the wall shear stress gradients.

4.1. Invariants of the velocity gradient tensor

Vessel non-planarity and vessel curvature have long been acknowledged to play an important role in physiological flows [1] and known to form vortical structures [33]. These tend to be the dominant structures in physiological flows, which do not commonly exhibit turbulence, and affect the flow stability as well as mixing and other transport properties [4,3]. Vortices have been widely studied with a range of criterion to extract both the surface as well as the core line, with the most widely used in 3-dimensional studies being the λ_2 criterion [34], the Q criterion [35], the Δ criterion [36] which are based on the velocity gradient tensor or its symmetric and antisymmetric parts [34,37], as well as other measures such as the helicity [38] and the vorticity magnitude. Other notions of coherent structures are defined by the finite-time Lyapunov exponent [39,40] and the closely related Lagrangian coherent structures [41,42].

In this work we will discuss the computed flow field using the velocity gradient tensor due to the simplicity, ease of calculation and detail of insight that can be obtained. The analysis remains local however, such that time integrated effects and structures should be described by particle tracking or other means.

Let us consider a flow field free of singular cases such as shocks and vortex sheets. A Taylor series can be used to expand the velocity in terms of the spatial coordinate around an arbitrary point O in the flow field. This is equivalent to performing a perturbation of the velocity field with respect to the spatial coordinates.

$$u_i = \dot{x}_i = A_i + A_{ij}x_j + A_{ijk}x_j x_k + \cdots, \quad i,j,k = 1,\ldots,3, \tag{1}$$

where A_{ij} is the velocity gradient tensor given by

$$\mathbf{A} = A_{ij} = (\nabla \mathbf{u}) = \frac{\partial u_i}{\partial x_j} = u_{i,j}, \quad i,j = 1,\ldots,3. \tag{2}$$

Note that the velocity gradient tensor can be written as $\mathbf{A} = \frac{\partial u_j}{\partial x_i} = u_{j,i}$ elsewhere in the literature [43,44].

If the coordinate system is assumed to translate without rotation, with the origin following a passive particle trace, then the origin is a critical point location. In this frame of reference $A_i = 0$, and if O is on a no-slip boundary, then also $A_{ij} = 0$.

Truncating second and higher order terms in Eq. (1) results in a linear system of ODEs, hence $\dot{\mathbf{x}} = \mathbf{A}\cdot\mathbf{x}$, or explicitly

$$\begin{pmatrix} \dot{x}_1 \\ \dot{x}_2 \\ \dot{x}_3 \end{pmatrix} = \begin{pmatrix} u_{11} & u_{12} & u_{13} \\ u_{21} & u_{22} & u_{23} \\ u_{31} & u_{32} & u_{33} \end{pmatrix} \begin{pmatrix} x_1 \\ x_2 \\ x_3 \end{pmatrix}, \tag{3}$$

whose solution involves either real or imaginary eigenvalues (λ_i, $i = 1,\ldots,3$):

$$\begin{cases} x_1(t) = x_1(0)e^{\lambda_1 t}, \\ x_2(t) = x_2(0)e^{\lambda_2 t}, \\ x_3(t) = x_3(0)e^{\lambda_3 t}, \end{cases} \quad \begin{cases} x_1(t) = x_1(0)e^{\lambda_1 t}, \\ x_2(t) = e^{\lambda_2 t}[x_2(0)\cos(\lambda_3 t) + x_3(0)\sin(\lambda_3 t)], \\ x_3(t) = e^{\lambda_2 t}[x_3(0)\cos(\lambda_3 t) - x_2(0)\sin(\lambda_3 t)]. \end{cases} \tag{4}$$

These are the local instantaneous streamlines, hence describing locally the motion of the flow. In unsteady flow, the expansion in Eq. (1) is applied at a moment in time, such that the solution trajectories correspond to particle paths, which do not generally coincide with streamlines except at an instant. These analytic solution trajectories have been used in particle tracing for linear tetrahedral elements [45] and tracing stream-surfaces [46].

For clarity we will order the eigenvalues such that, if they are all real then $\lambda_1 \geqslant \lambda_2 \geqslant \lambda_3$, while if the solution comprises of a real and complex conjugate pair then λ_1 is real and the complex conjugate pair is given by $\lambda_2 \pm i\lambda_3$. The corresponding unit eigenvectors are denoted by $\zeta_1, \zeta_2, \zeta_3$. The eigenvectors indicate the principal directions of motion of the flow surrounding the critical point, hence they define the planes in which the solution locally osculates, see Fig. 2. In the case of three real eigenvalues, the solution trajectories osculate three distinct planes, while if the solution involves a complex eigenvalue, only one plane exists, given by the eigenvectors of the complex conjugate eigenvalues. In this case the plane defines the plane of rotation, while the eigenvector associated to the real eigenvalue indicates the local axis of swirling. It is important to note that the eigenvectors need not be orthogonal except in the case of irrotational flow.

In the case of an incompressible flow, the trace of the velocity gradient tensor is $tr(\nabla\mathbf{u}) = \partial u_1/\partial x_1 + \partial u_2/\partial x_2 + \partial u_3/\partial x_3 = 0 = \lambda_1 + \lambda_2 + \lambda_3$ ($= \lambda_1 + 2\lambda_2$ if complex). Furthermore the ratio of the eigenvalues, if real will indicate the level of stretching and compressing of the flow along the eigenvectors, and if complex provide the spiralling compactness by λ_2/λ_3, since from Eq. (4) the time period of one revolution in the spiralling plane is given by $2\pi/\lambda_3$ [37].

By tracking a passive particle path and plotting the associated eigenvectors, one can perceive the local dynamics surrounding the trajectory. In Fig. 2 detail of a passive particle trajectory is shown in the region of a vortex structure such that there is a real and complex conjugate pair of eigenvalues. The local osculating plane and axis of swirling are superposed on the detail of the particle trajectory.

Given eigenvalues λ_1, λ_2, λ_3 of the velocity gradient tensor $\mathbf{A} = \nabla\mathbf{u}$, the eigenvalue problem $[\mathbf{A} - \lambda_i I]\zeta_i = 0$, $i = 1,\ldots,3$, where ζ_i is the eigenvector associated to λ_i, can be determined solving the characteristic equation $\det[\mathbf{A} - \lambda_i I] = 0$. For a 3×3 matrix as is our case, this can be written as

$$\lambda_i^3 + P\lambda_i^2 + Q\lambda_i + R = 0, \quad i = 1,\ldots,3, \tag{5}$$

where P, Q and R are the variants

$$\begin{aligned} P &= -(u_{11} + u_{22} + u_{33}) = -tr(\mathbf{A}), \\ Q &= \begin{vmatrix} u_{11} & u_{12} \\ u_{21} & u_{22} \end{vmatrix} + \begin{vmatrix} u_{11} & u_{13} \\ u_{31} & u_{33} \end{vmatrix} + \begin{vmatrix} u_{22} & u_{23} \\ u_{32} & u_{33} \end{vmatrix}, \\ R &= \begin{vmatrix} u_{11} & u_{12} & u_{13} \\ u_{21} & u_{22} & u_{23} \\ u_{31} & u_{32} & u_{33} \end{vmatrix} = -\det[\mathbf{A}]. \end{aligned} \tag{6}$$

The surface that divides the real from complex solutions of the eigenvalues can be shown to be $27R^2 + (4P^3 - 18PQ)R + (4Q^3 - P^2Q^2) = 0$ [47]. For incompressible flow however $P = 0$ and the divisory line in the $Q - R$ plane becomes $\frac{27}{4}R^2 + Q^3 = 0$, as shown in Fig. 2. In this way the invariants Q and R can be used directly to describe the flow field.

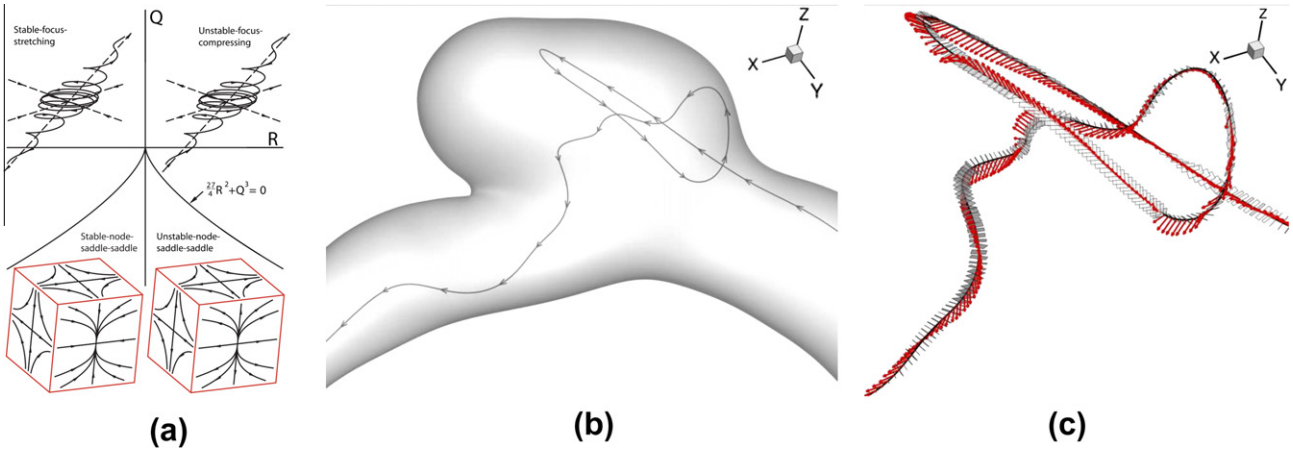

Fig. 2. (a) Solution trajectories can be either node–saddle–saddle or focus-stretching, as well as either stable or unstable. The axes are the eigenvectors of the velocity gradient tensor. (b) Sample trajectory for steady-state computations of patient Case 1 and (c) region detail of trajectory in a vortical structure showing the plane of swirling and the axis of stretching, given by the eigenvectors of the velocity gradient tensor.

The velocity gradient tensor can be split into a symmetric and antisymmetric part, corresponding to rate-of-strain and rate-of-rotation tensors, hence $\nabla \mathbf{u} = \partial u_i/\partial x_j = S_{ij} + W_{ij}$, $i, j = 1, \ldots, 3$, where $S_{ij} = (\partial u_i/\partial x_j + \partial u_j/\partial x_i)/2$ and $W_{ij} = (\partial u_i/\partial x_j - \partial u_j/\partial x_i)/2$. Following the analysis above, the invariants of S_{ij} are Q_S and R_S, while the invariant of W_{ij} is Q_W, noting that P, P_S, P_W and $R_W = 0$ for an incompressible flow. Physical meaning to these invariants is briefly given as follows [48]: $Q = Q_S + Q_W$ is a measure of the rate of rotation over strain rate; $Q_S \propto$ rate of viscous dissipation of kinetic energy, $Q_W \propto$ vorticity intensity, positive R_S is associated with sheet-like structures, and negative R_S to tube-like structures. These invariants are widely used in the study of fluid mechanics and turbulence, see [48] and references therein.

Other measures of describing the flow field are varied, including vorticity stretching [49] or lumped vorticity rings [43]. Since the circulation is constant for a closed curve group of fluid elements in the absence of rotational external forces, from Kelvin's law, a corollary from Helmholtz second law, and also from Helmholtz first law stating that the strength of a vortex filament is constant along its length then, tracking the lumped vorticity ring over limited distances (before large distortions occur) will allow for a qualitative representation of the flow dynamics with respect to the vortex structure. As stated in [43] the tracking of this lumped vortex ring (or set of rings) of iso-vorticity at the inlet allows for a clear identification of rapid stretching and hence the behaviour of the vorticity and the vortex structures.

It should be noted that in the case of linear tetrahedral elements, the velocity gradient tensor is constant over the element, and facilitates the post-processing considerably. It is in fact this property that is often used in extracting the vortex cores. A number of methods exist in extracting the vortex cores, however the most popular are based on the reduced velocity in the element [50,51] and the higher order method approach [52]. Here we introduce a further method that is less computationally expensive and is based once again on the velocity gradient tensor [25,46]. In [25], the set of possible solutions of the eigenvalues for a linear tetrahedral element is presented, with a corresponding discussion of existence of a unique critical point and degenerate cases. In the case of a swirling flow such that the dynamics involves an osculating plane and an axis of rotation, the eigenvalues of the velocity gradient tensor are λ_1, $\lambda_2 \pm i\lambda_3$. Two solutions are admissible, $\lambda_1 = 0$, $\lambda_2 \pm i\lambda_3$, $\lambda_3 \neq 0$ for which no unique critical point exists and the motion is circular around the axis, and $\lambda_1 \neq 0$, $\lambda_2 \pm i\lambda_3$, $\lambda_3 \neq 0$ in which the motion is spiralling about the axis and a critical point does exist. The identification of the vortex core relies on noting if the axis of rotation passes through the tetrahedron element under consideration, which can readily be performed based on barycentric coordinates or intersection with the tetrahedral's four planar triangle faces. The result is a set of points (at least one per tetrahedron) that can be connected based on the existence of a point in a neighbouring tetrahedron element, though this has not been performed in the current work. This method is sensitive to noisy data (since the gradients of velocity are obtained from a piecewise linear field) and certain spurious disconnected points can be obtained.

4.2. Invariants of the wall shear stress gradient tensor

A similar analysis can be performed using the wall shear stress on the walls of the domain instead of the velocity field [53]. This is performed by firstly projecting the wall shear stress onto two orthogonal directions (hence local 2-dimensional coordinates) for each triangle mesh element that defines the bounding geometry. Considering now this projected wall shear stress field for each element, a similar Taylor expansion as in Eq. (3), truncated to include only the first term, can be used to obtain a set of two first-order ODEs. Since the triangle elements are piecewise-linear and hence planar, the analysis is essentially 2-dimensional. The critical point analysis can be then performed and a full description of the permissible sets of eigenvalues for a 2-dimensional case of a linearly varying field is also discussed in [25]. The critical points can be either foci or saddle configurations, where the foci can have two real eigenvalues or a complex conjugate pair.

In doing so the near-wall flow parallel to the wall can be described concisely and elegantly. For critical points with a real set of eigenvalues, a point a small distance along the eigenvectors can also be plotted in order to identify the principal directions of the motion visually. These points can be used as seeding locations for integration of the wall shear stress on the surface to obtain surface shear lines (sometimes termed 'limiting streamlines', 'surface streamlines' or 'skin-friction lines' elsewhere in the literature), hence the lines that are aligned to the tangential component of the viscous traction exerted by the flow on the wall. This leads to a minimal set of surface shear lines (since they must start and end at a critical point, principal directions bound a region, and the lines cannot cross each other) that describe the tangential components of the flow near the wall, and are important in identifying features such as regions of flow separation and impingement.

It should be noted that this wall shear stress critical points analysis in the 2-dimensional case on the wall is a simpler approach to discuss the 3-dimensional flow field close to the wall. For example

a complex conjugate pair of eigenvalues identifies where a vortex structure is rooted at the wall, a set of real positive eigenvalues indicates a point of flow impingement (and point flow separation if both negative, though this is in practice not common) and a saddle configuration (one positive and one negative real eigenvalues) often indicates a point on a line of flow separation. Examples of separation schematics can be found in [54–57]. Fig. 3 shows detail of steady-state simulations of Case 1 at the distal region of the aneurysm neck. Critical points of the wall shear stress are identified and surface shear lines are plotted, which together map clearly the near-wall fluid dynamics tangential to the wall.

4.3. Near-wall convective transport

The above discussion has looked at describing the free-slip flow field and the tangential component of the flow field near the wall. In this section we discuss the near-wall transport perpendicular to the wall, that is of importance in physiological flows from the stand point of exchange processes and interactions between flow and wall. The near-wall convective transport normal to the wall discussed here describes how the flow moves from or returns to the surface gradually. The method follows the work of [26], in which the values of low WSS and transport to the wall were correlated to inwards vascular remodelling for two post-operative peripheral bypass grafts.

For gradual convective transport normal to the wall, a measure of the strength is given by the surface shear line convergence (or separation) [56]. This observation was first explained in [57,58] by considering Fig. 4 as follows: let the flow be steady and incompressible, then mass flux is constant and is given by $\dot{m} = \rho ab\bar{\mathbf{u}}$, where $\bar{\mathbf{u}}$ is the mean velocity of the cross section. Considering the cross section to be small such that the wall shear stress magnitude is given by $\tau_w = \mu(\frac{2\bar{\mathbf{u}}}{a})$, where μ is the dynamic viscosity, and substituting we obtain:

$$\dot{m} = \text{constant} = \frac{a^2 b \tau_w \rho}{2\mu}. \tag{7}$$

Rewriting this we find that $a \propto (b\tau_w)^{-1/2}$; hence for a constant wall shear stress magnitude, the convective transport normal to the wall is inversely proportional to the root of the distance between the surface shear lines. The coalescence or separation of the surface shear lines can therefore be an indication of flow moving from or returning to the surface. This approach is difficult to use quantitatively in practice as it requires information of relative position of traced points along the surface shear lines.

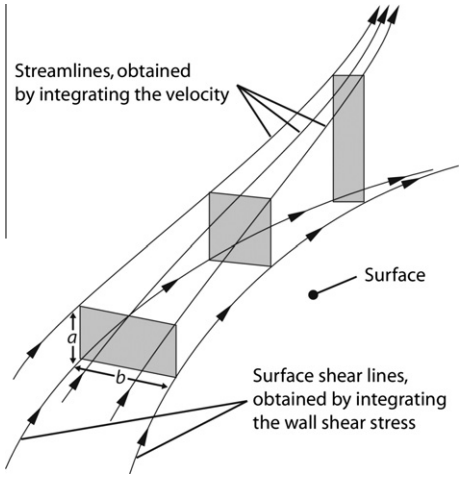

Fig. 4. Surface shear lines, obtained by integrating the traction force components on the wall, coalesce (or diverge) and due to continuity the fluid moves away (or towards) the wall gradually, such that $a \propto (b\tau_w)^{-1/2}$, from Eq. (7), where τ_w is the wall shear stress magnitude.

A different approach to describe the near-wall convective transport is derived by considering a series expansion of Lagrangian dynamics of a fluid. The approach used follows closely that of [26] and is presented in terms of the wall shear stress gradients. Near-wall residence times and convective transport parallel to the wall are also linked to the wall shear stress. A brief derivation is now given.

Imagine a flow with velocity $\mathbf{u}(\mathbf{x},t) = (u(\mathbf{x},t), v(\mathbf{x},t), w(\mathbf{x},t))$ over a wall and let $(\underline{i},\underline{j},\underline{k})$ denote the unit vectors in the (x,y,z) directions respectively. Let us consider a point on the wall with position vector $\mathbf{x}_{0w} = (0,0,0)$ and select a particle at time $t = t_0$ released from an initial position $\mathbf{x}_0 = (\delta x, \delta y, \delta z)$, then after a short time δt the separation of the particle from its initial position can be expressed by a Taylor series expansion in time, given by

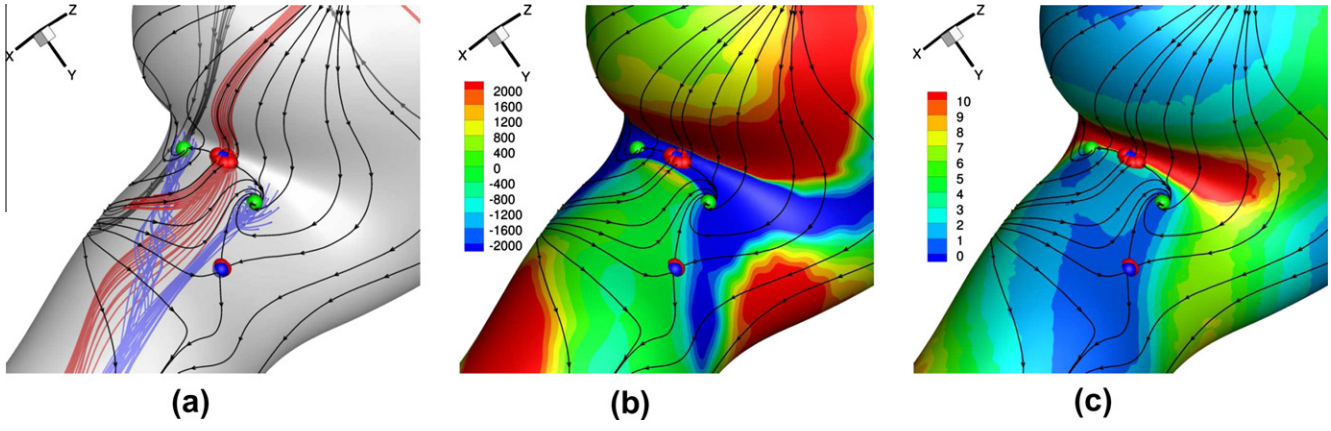

Fig. 3. Detail of distal aneurysm neck region of steady-state computations for Case 1. The images show surface shear lines and WSS critical points, which are coloured such that green indicates a complex conjugate pair solution (spiralling motion), blue indicates real solutions and red are locations a small distance along the eigenvectors (hence principal directions. (a) Passive particle streamlines in the fluid domain indicate flow separation (red) and vortex cores touching the wall (blue) which are also identified by the WSS critical points. (b) Plot of TR (Pa m^{-1}) as the convective transport normal where positive values indicate flow movement to the wall and negative is movement away from the wall. The region of flow separation is marked as strong movement away from the wall for example. (c) Plot of WSS (Pa) and describes the convective transport parallel to the wall. (For interpretation of the references to colour in this figure legend, the reader is referred to the web version of this article.)

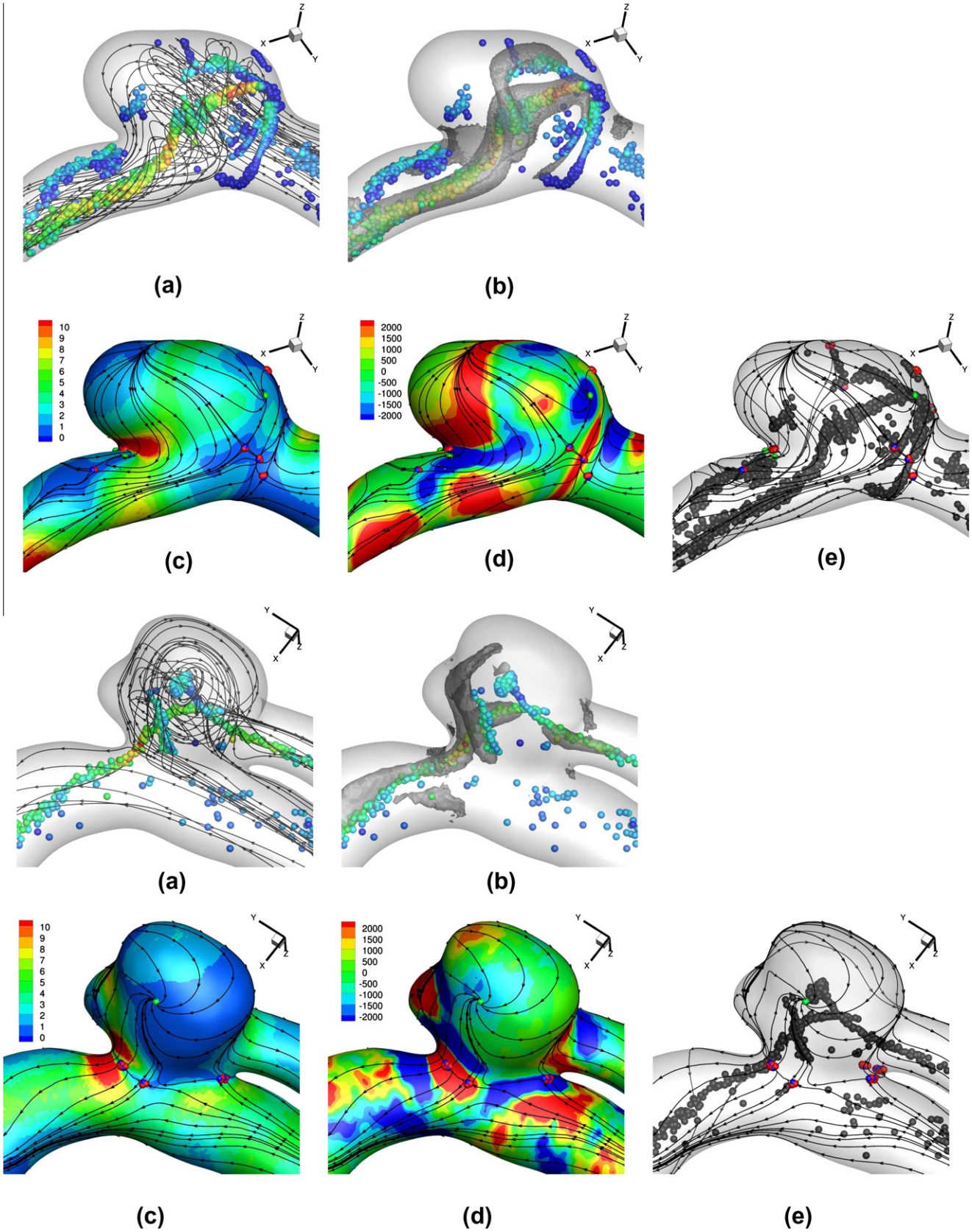

Fig. 5. Steady-state computations for Case 1 (top) and Case 2 (bottom). (a) Streamlines and vortex core points coloured by the magnitude of the complex eigenvalue (λ_3) of the velocity gradient tensor, hence the rate swirling. (b) Vortex core points and iso-surfaces of $\lambda_2 = -10^4$ for vortex identification [34]. Plots of surface shear lines and WSS critical points (same colouring scheme as in Fig. 3) and (c) plot of WSS (Pa), (d) TR (Pa m^{-1}), (e) vortex core points. (For interpretation of the references to colour in this figure legend, the reader is referred to the web version of this article.)

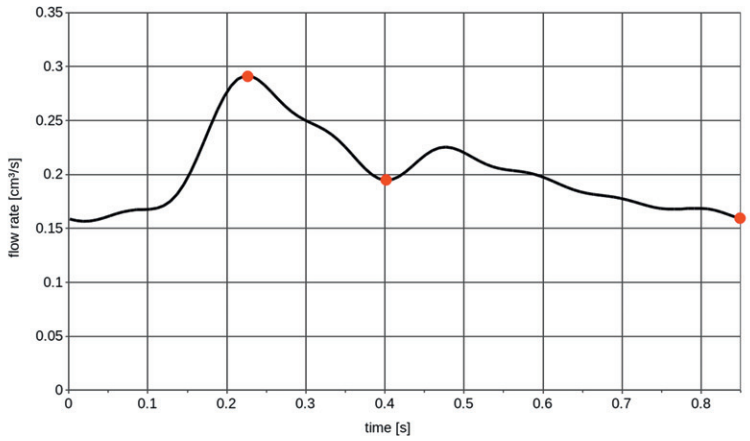

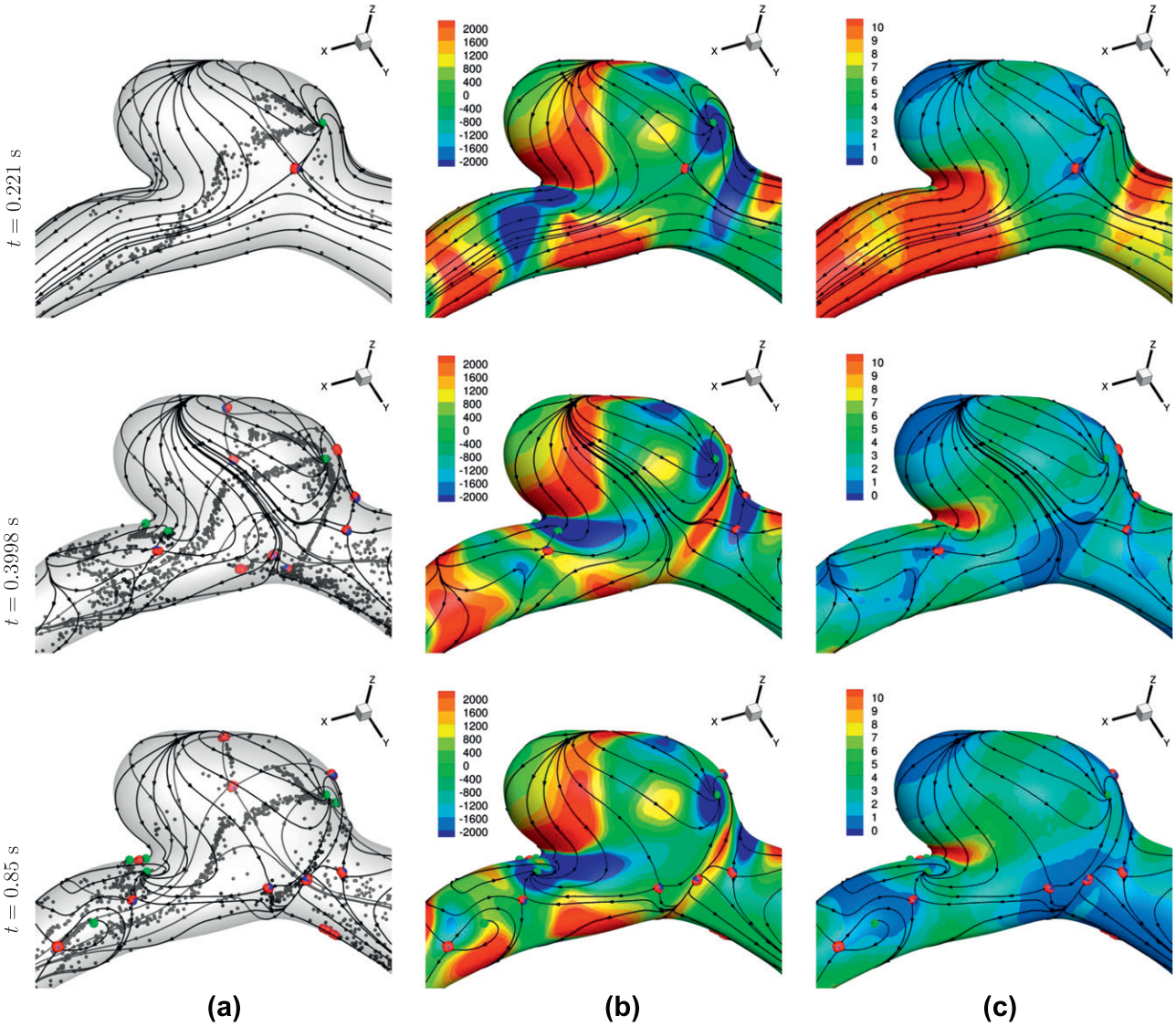

Fig. 6. Top row: cardiac cycle at the inflow section and the three locations for which the results are presented. Plots of surface shear lines and WSS critical points (same colouring scheme as in Fig. 3) and (a) vortex core points, (b) TR (Pa m^{-1}), (c) WSS (Pa). (For interpretation of the references to colour in this figure legend, the reader is referred to the web version of this article.)

$$\mathbf{x}(t_0+\delta t)-\mathbf{x}(t_0)=\delta t\left(\frac{d\mathbf{x}}{dt}\right)\Big|_{\mathbf{x}_0,t_0}+\frac{1}{2}\delta t^2\left(\frac{d^2\mathbf{x}}{dt^2}\right)\Big|_{\mathbf{x}_0,t_0}+O(\delta t^3), \tag{8}$$

$$\begin{aligned}\left(\tfrac{d\mathbf{x}}{dt}\right)\big|_{\mathbf{x}_0,t_0}&=\mathbf{u}(\mathbf{x}_0,t_0),\\ \left(\tfrac{d^2\mathbf{x}}{dt^2}\right)\Big|_{\mathbf{x}_0,t_0}&=\left(\tfrac{d\mathbf{u}}{dt}\right)\big|_{\mathbf{x}_0,t_0}=\left(\tfrac{\partial\mathbf{u}}{\partial t}+\mathbf{u}\cdot\nabla\mathbf{u}\right)\big|_{\mathbf{x}_0,t_0}.\end{aligned} \tag{9}$$

where

To simplify the expansion further we now consider the wall to be in the $x-y$ plane such that the surface normal is the z direction. The velocity at a point near the wall $\mathbf{x}_0 = \mathbf{x}_{0w} + \delta\mathbf{x}$ can be expanded using a Taylor series expansion in space. Remembering that the velocity components at the wall are zero, the spatial gradients in the plane of the wall are zero, from continuity $\partial u/\partial x + \partial v/\partial y + \partial w/\partial z = 0$, and hence also $\partial w/\partial z = 0$, then we obtain

$$\mathbf{u}(\mathbf{x}_0, t_0) = \left(\delta z\left(\frac{\partial u}{\partial z}\right)\Big|_{\mathbf{x}_{0w},t_0} + \frac{1}{2}\delta z^2\left(\frac{\partial^2 u}{\partial z^2}\right)\Big|_{\mathbf{x}_{0w},t_0}\right) \times \underline{i}\left(\delta z\left(\frac{\partial v}{\partial z}\right)\Big|_{\mathbf{x}_{0w},t_0} + \frac{1}{2}\delta z^2\left(\frac{\partial^2 v}{\partial z^2}\right)\Big|_{\mathbf{x}_{0w},t_0}\right)\underline{j}\left(\frac{1}{2}\delta z^2\left(\frac{\partial^2 w}{\partial z^2}\right)\Big|_{\mathbf{x}_{0w},t_0}\right)\underline{k}. \tag{10}$$

Making one final substitution by rewriting the velocity derivatives for a Newtonian flow in terms of the wall shear stress components

$$\frac{\tau_x}{\mu} = \left(\frac{\partial u}{\partial z}\right)\Big|_{\mathbf{x}_{0w},t_0}; \quad \frac{\tau_y}{\mu} = \left(\frac{\partial v}{\partial z}\right)\Big|_{\mathbf{x}_{0w},t_0} \tag{11}$$

we can then expand $\mathbf{x}(t_0+\delta t) - \mathbf{x}(t_0)$ from Eq. (8) in its terms of the Taylor series expansion up to second order terms, distinguishing the components in the direction parallel and normal to the wall

$$\begin{aligned}
&\mathbf{x}(t_0+\delta t) - \mathbf{x}(t_0) = \\
&O(\delta t\cdot\delta z): && \left(\tfrac{\tau_x}{\mu}\right)\underline{i} + \left(\tfrac{\tau_y}{\mu}\right)\underline{j},\\
&O(\delta t\cdot\delta z^2): && \tfrac{1}{2\mu}\left(\left(\tfrac{\partial\tau_x}{\partial z}\right)\underline{i} + \left(\tfrac{\partial\tau_y}{\partial z}\right)\underline{j}\right) - \tfrac{1}{2\mu}\left(\tfrac{\partial\tau_x}{\partial x} + \tfrac{\partial\tau_y}{\partial y}\right)\underline{k},\\
&O(\delta t^2\cdot\delta z): && \tfrac{1}{2\mu}\left(\left(\tfrac{\partial\tau_x}{\partial t}\right)\underline{i} + \left(\tfrac{\partial\tau_y}{\partial t}\right)\underline{j}\right),\\
&O(\delta t^2\cdot\delta z^2): && \tfrac{1}{2\mu}\left(\tau_x\tfrac{\partial\tau_x}{\partial x} + \tau_y\tfrac{\partial\tau_x}{\partial y} + \tfrac{\partial^2\tau_x}{\partial z\partial t}\right)\underline{i}\\
& && + \tfrac{1}{2\mu}\left(\tau_x\tfrac{\partial\tau_y}{\partial x} + \tau_y\tfrac{\partial\tau_y}{\partial y} + \tfrac{\partial^2\tau_y}{\partial z\partial t}\right)\underline{j}\\
& && + \tfrac{1}{2\mu}\left(\tfrac{\partial^2\tau_x}{\partial x\partial t} + \tfrac{\partial^2\tau_y}{\partial y\partial t}\right)\underline{k}.
\end{aligned} \tag{12}$$

From this the dominant component parallel and normal to the wall are time independent and given by

$$\begin{aligned}
(\mathbf{x}(t_0+\delta t) - \mathbf{x}(t_0))\underline{i} &= (\delta t\cdot\delta z)\left(\tfrac{\tau_x}{\mu}\right),\\
(\mathbf{x}(t_0+\delta t) - \mathbf{x}(t_0))\underline{j} &= (\delta t\cdot\delta z)\left(\tfrac{\tau_y}{\mu}\right),\\
(\mathbf{x}(t_0+\delta t) - \mathbf{x}(t_0))\underline{k} &= -\tfrac{1}{2\mu}(\delta t\cdot\delta z^2)\left(\tfrac{\partial\tau_x}{\partial x} + \tfrac{\partial\tau_y}{\partial y}\right).
\end{aligned} \tag{13}$$

Eq. (13) states that the steady-state near-wall convective transport parallel to the wall is proportional to the tangential wall shear stress components, while the transport normal to the wall is proportional to the spatial gradients of wall shear stress in the plane of the wall. Together, the directional components give an indication of the local near-wall residence times.

Studies on flow-mediated mechanotransduction suggest that sensed haemodynamic stresses generate signals and responses from a biochemical perspective, indicating an adaptive auto-regulation to local factors [18,19,59,60,11]. The sensory mechanisms are usually attributed to the endothelial cells typically concerning changes in the flow or abnormal flow patterns, discussed commonly in terms of wall shear stress and derived parameters (such as WSS spatial and temporal gradients), which can stimulate proliferation, permeability and migration. Sensory mechanisms for the endothelial cells to feel these alteration in the wall shear stress and the spatial gradients of wall shear stress have long been sought, however from Eq. (13) these are easily identified physically from the components of the near-wall velocity: the tangential component is related to shear while the vertical to a change in momentum. A greater number of parameters are feasibly detectable by the endothelial cells (even if currently the mechanisms and pathways may still be unknown), such as the temporal gradients of wall shear stress, and importantly these can be related to near-wall transport mechanics from Eq. (12).

In the results discussed below, the strength of the near-wall convective transport normal to the wall is identified by the quantity

$$TR = \frac{\partial\tau_{\zeta_1}}{\partial\zeta_1} + \frac{\partial\tau_{\zeta_2}}{\partial\zeta_2}, \tag{14}$$

where $\tau_{\zeta_1}/\mu = \vec{n}\cdot\nabla(\mathbf{u}\cdot\vec{\zeta_1})$ and $\tau_{\zeta_2}/\mu = \vec{n}\cdot\nabla(\mathbf{u}\cdot\vec{\zeta_2})$, with $\vec{\zeta_1}$ and $\vec{\zeta_2}$ as the perpendicular unit tangent vectors and $\vec{n}$ as the unit normal vector to the individual triangular surface elements. In this way the triangular faces are considered individually to calculate the WSS gradients as a post-processing step, and an average at the element vertices is then performed considering all adjacent elements since the spatial gradients will be discontinuous across the elements. In this work the convention of negative values of TR indicates convective transport from the wall, and positive values indicate transport to the wall. The results of TR can be used in conjunction to the surface shear lines coalescence or separation for easy of interpretation if required, however this is valid in regions of relatively constant wall shear stress. Example of the use of TR is shown in Fig. 3, in which region of flow separation at the distal region of the aneurysm neck is identifiable easily, as well as other flow features.

An important feature of this analysis is that, using derivatives of the fluid mechanic properties on the wall and relating them to the transport, near-wall free-slip flow field can be approximated by integrating the derivatives, and examples of this are shown in [26].

5. Results

Applying the above methods to the steady-state simulations for both patient Cases and the time-periodic simulation of patient Case 1, the free-slip and no-sip regions are now analysed. We first present the steady-state solutions using the methods discussed above to describe the key flow features in the free-slip domain and importantly how these are related to the no-slip domain. The results of these steady-state simulations are shown in Fig. 5 for both Cases and those of the unsteady simulations are shown in Fig. 6. The vortex core points appear unaligned and some single dispersed points are identified in the flow field erroneously; this has been identified to be due to the interpolation of cell-centered data obtained from the finite volume computations onto a node-centered data used in the analysis, and from the numerical accuracy of the computational result from which the post-processing of derivatives leads to additional errors.

Two important points are first addressed from the results of Fig. 5: firstly the use of streamlines to describe the flow field, as discussed in [16] with relation to correlation to aneurysm rupture, can be rather difficult to discern and classify and a less cluttering approach is needed; secondly the λ_2 criterion for vortex structure identification does not align in fact to the vortex cores. This second point can lead to misleading conclusions about the flow structures, the reason for this is due to the viscous terms in the Navier–Stokes equations, and discussed in greater detail in [36], such that a pressure minimum in the plane (which is the basis of the λ_2 criterion [34,43]) may not be appropriate.

The surface shear lines and the critical points of the WSS, in conjunction to plots of the WSS and TR, can be used to describe the no-slip domain entirely. The critical points of the WSS act as dividing lines to the surface shear lines, bounding these to common regions. The critical points furthermore identify locations of flow separation and impingement, and the type, i.e. if a vortex is rooted at the wall or a simpler arrangement is present. The WSS

and TR locally identify the velocity of the fluid near the wall, in the tangential and normal directions. In this way a complete description of the no-slip domain is presented in a concise and physically intuitive form. The vortex core points, on the other hand, act as skeletonisations of the free-slip domain by identifying the axes of rotation (not always part of a vortex therefore), as well as other measures such as the rate of stretching, spiralling intensity and local osculating planes, if desired. The strongest vortex cores, that leave the aneurysm through the side branch or the main arterial vessel, appear to be anchored to the vessel wall, as seen from the critical points of the WSS. It is further possible to identify from the values of TR and the critical points of WSS the effect of the swirling motion in the flow field around the vortex cores; for example in the case of a vortex lying adjacent to the wall a net division of sign of TR is observed, while the surface shear lines would be at an angle to this division.

In Fig. 6 snapshots of the solution at three time intervals are presented. The interest is to identify clearly and easily the characteristics of the flow field. An interesting result that emerges is the relative constancy of TR during the cycle, while the WSS is seen to vary more noticeably. A further distinguishing feature is the persistence of the vortex core anchored to the proximal portion of the aneurysm dome (identified easily from the WSS critical points) and continues to the distal parent artery. During diastole the flow field in the aneurysm becomes more complex due to the fluid deceleration, as seen by an increased number of WSS critical points and vortex cores, however by the end of the diastolic phase (at the end of the heartbeat) the flow field has again become relatively simplified. A more in-depth analysis of the time snapshots will be interesting to identify the change in the WSS critical points and the vortex cores, the behaviour and stability of which may lead to correlation and classification of aneurysm rupture or growth directions.

6. Conclusion and future work

The local dynamics for both the free-slip and near-wall flow regions can be studied using the Taylor series expansion of the velocity, wall shear stress or relative position. This leads to a detailed local information of the flow field that can aid the discussion of fluid dynamic phenomena concisely. The use of these methods has been shown to provide a clear and in-depth description of the flow in two patient-specific geometries of saccular cerebral aneurysms. The description is similar to other works involving vortex stability during the cardiac cycle, wall shear stress magnitude and impingement size areas, however the approaches of extracting these results provided in this work have the advantage of being simple to calculate, provide a clear physical basis to the measures, are robust and avoid a large amount of clutter in the analysis that is otherwise inevitable.

The unsteady simulations and use of the above described methods, have identified that the WSS critical points (hence also the surface shear lines) alter noticeably during the cardiac cycle, however the transport normal to the wall and the dominant vortex core remain largely unaltered. The deceleration phase of the cardiac cycle causes a larger number of smaller vortices to be formed in the aneurysm. The region of flow separation at the aneurysm neck is not seen at the peak systole. Other flow features that can concisely describe the flow have also been discussed.

An important physical analysis of the WSS spatial and temporal gradients from Eq. (12) sheds light on widely used fluid dynamic parameters correlated to disease. These are related to the near-wall transport, and this physical interpretation can be linked to possible sensory mechanisms of the endothelial cells, and hence mechanotransduction and related biochemical signalling.

The analysis has been performed on cerebral aneurysms and can foreseeably be extended to study a greater number of geometries and applications to provide a more learned understanding of human physiology in normal and diseased states. Future work would primarily be use of a larger number of data sets in order extract correlations and statistical measures related to aneurysm growth and rupture.

Acknowledgements

We greatly acknowledge Prof. Jorge Campos, and his team from the Faculty of Medicine of the University of Lisbon, for providing us the in vivo rotational CTA scans of specific patients. This work has been partially funded by FCT (Fundação para a Ciência e Tecnologia, Portugal) through Grant SFRH/BPD/44478/2008, and through the Project UTAustin/CA/0047/2008.

References

[1] Caro CG, Doorly DJ, Tarnawski M, Scott KT, Long Q, Dumoulin CL. Non-planar curvature and branching of arteries and non-planar-type flow. Proc Math Phys Eng Sci 1996;452(1944):185–97.
[2] Giordana S, Sherwin SJ, Peiró J, Doorly DJ, Crane JS, Lee KE, et al. Local and global geometric influence on steady flow in distal anastomoses of peripheral bypass grafts. J Biomech Eng 2005;127(7):1087–98.
[3] Cookson AN, Doorly DJ, Sherwin SJ. Mixing through stirring of steady flow in small amplitude helical tubes. Ann Biomed Eng 2009;17(4):710–21.
[4] Pitt R. Numerical simulations of fluid mechanical phenomena in idealised physiological geometries: stenosis and double bend. PhD thesis, Aeronautical Engineering, Imperial College, University of London, UK; 2007.
[5] Gambaruto AM, Moura A, Sequeira A. Topological flow structures and stir mixing for steady flow in a peripheral bypass graft with uncertainty. Int J Numer Meth Biomed Eng 2010;26(7):926–53.
[6] Lee KE, Parker KH, Caro CG, Sherwin SJ. The spectral/hp element modelling of steady flow in non-planar double bends. Int J Numer Meth Fluids 2008;57(5):519–29.
[7] Krex D, Schackert HK, Schackert G. Genesis of cerebral aneurysms – an update. Acta Neurochir 2001;143(5):429–49.
[8] Jamous MA, Nagahiro S, Kitazato KT, Satoh K, Satomi J. Vascular corrosion casts mirroring early morphological changes that lead to the formation of saccular cerebral aneurysms: an experimental study in rats. J Neurosurg 2005;102:532–5.
[9] Shimogonya Y, Ishikawa T, Imai Y, Matsuki N, Yamaguchi T. Can temporal fluctuation in spatial wall shear stress gradient initiate a cerebral aneurysm? A proposed novel hemodynamic index, the gradient oscillatory number (GON). J Biomech 2009;42(4):550–4.
[10] Kulcsár Z, Ugron A, Marosfõi M, Berentei Z, Paál G, Szikora I. Hemodynamics of cerebral aneurysm initiation: the role of wall shear stress and spatial wall shear stress gradient. Am J Neuroradiol 2010;32:587–94.
[11] Meng H, Wang Z, Hoi Y, Gao L, Metaxa E, Swartz DD, et al. Complex hemodynamics at the apex of an arterial bifurcation induces vascular remodeling resembling cerebral aneurysm initiation. Stroke 2007;38:1924–31.
[12] Mantha A, Karmonik C, Benndorf G, Strother C, Metcalfe R. Hemodynamics in a cerebral artery before and after the formation of an aneurysm. Am J Neuroradiol 2006;27(5):1113–8.
[13] Baek H, Jayaraman MV, Richardson PD, Karniadakis GE. Flow instability and wall shear stress variation in intracranial aneurysms. J Roy Soc Interf 2010;7(47):967–88.
[14] Ojha M. Wall shear stress temporal gradient and anastomotic intimal hyperplasia. Circul Res 1994;74:1227–31.
[15] Nixon AM, Gunel M, Sumpio BE. The critical role of hemodynamics in the development of cerebral vascular disease. J Neurosurg 2010;112:1240–53.
[16] Cebral JR, Castro MA, Burgess JE, Pergolizzi RS, Sheridan MJ, Putman CM. Characterization of cerebral aneurysms for assessing risk of rupture by using patient-specific computational hemodynamics models. Am J Neuroradiol 2005;26:25502559.
[17] Sforza DM, Putman CM, Cebral JR. Hemodynamics of cerebral aneurysms. Ann Rev Fluid Mech 2009;41:91–107.
[18] Orr AW, Helmke BP, Blackman BR, Schwartz MM. Mechanisms of mechanotransduction. Dev Cell 2006;10:11–20.
[19] Davies PF. Flow-mediated endothelial mechanotransduction. Physiol Rev 1995;75(3):519–60.
[20] Reneman RS, Arts T, Hoeks APG. Wallshear stress – an important determinant of endothelial cell function and structure - in the arterial system in vivo. J Vasc Res 2006;43:251–69.
[21] Sangalli LM, Secchi P, Vantini S, Veneziani A. A case study in explorative functional data analysis: geometrical features of the internal carotid artery. Technical report TR-2007-027, Mathematics and Computer Science, Emory University; 2007.

[22] Weir B, Amidei C, Kongable G, Findlay JM, Kassell NF, Kelly J, et al. The aspect ratio (dome/neck) of ruptured and unruptured aneurysms. J Neurosurg 2003;99:447–51.
[23] Piccinelli M, Hoi Y, Steinman D, Veneziani A, Antiga L. Automatic neck plane detection and 3D geometric characterization of aneurysmal sacs. Technical report TR-2011-013, Mathematics and Computer Science, Emory University; 2011.
[24] Chong MS, Perry AE. A general classification of three-dimensional flow fields. Phys Fluids A 1990;2(5):765–77.
[25] Nielson MN, Jung IH. Tools for computing tangent curves for linearly varying vector fields over tetrahedral domains. IEEE Trans Vis Comput Graph 1999;5(4):360–72.
[26] Gambaruto AM, Doorly DJ, Yamaguchi T. Wall shear stress and near-wall convective transport: comparisons with vascular remodelling in a peripheral graft anastomosis. J Comput Phys 2010;229(14):5339–56.
[27] Cebral JR, Castro MA, Appanaboyina S, Putman CM, Millan D, Frangi AF. Efficient pipeline for image-based patient-specific analysis of cerebral aneurysm hemodynamics: technique and sensitivity. IEEE Trans Med Imag 2005;24(4):457–67.
[28] Antiga L, Piccinelli M, Botti L, Ene-Iordache B, Remuzzi A, Steinman DA. An image-based modeling framework for patient-specific computational haemodynamics. Med Biol Eng Comput 2008;46(11):1097–112.
[29] Gambaruto AM, Peiró J, Doorly DJ, Radaelli AG. Reconstruction of shape and its effect on flow in arterial conduits. Int J Numer Meth Fluids 2008;57(5):495–517.
[30] <www.openfoam.org>.
[31] Cebral JR, Castro MA, Putman CM, Alperin N. Flow–area relationship in internal carotid and vertebral arteries. Physiol Meas 2008;29(5):585–94.
[32] Geuzaine C, Remacle JF. Gmsh: a three-dimensional finite element mesh generator with built-in pre- and post-processing facilities. Int J Numer Meth Eng 2009;79(11):1309–31.
[33] Dean WR. The stream-line motion of fluid in a curved pipe. Philos Mag 1928;5(30):673–95.
[34] Jeong J, Hussain F. On the identification of a vortex. J Fluid Mech 1995;285:69–94.
[35] Hunt JCR, Wray AA, Moin P. Eddies, streams, and convergence zones in turbulent flows. Studying turbulence using numerical simulation databases, 2. In: Proceedings of the 1988 summer program; 1988. p. 193–208.
[36] Perry AE, Chong MS. A description of eddying motions and flow patterns using critical-point concepts. Ann Rev Fluid Mech 1987;19:125–55.
[37] Chakraborty P, Balachandar S, Adrian RJ. On the relationships between local vortex identification schemes. J Fluid Mech 2005;535:189–214.
[38] Levy Y, Degani D, Seginer A. Graphical visualization of vortical flows by means of helicity. Am Inst Aeronaut Astronaut 1990;28(8):1347–52.
[39] Wolf A, Swift JB, Swinney HL, Vastano JA. Determining Lyapunov exponents from a time series. Physica D 1985;16:285–317.
[40] Boffetta G, Lacorata G, Redaelli G, Vulpiani A. Detecting barriers to transport: a review of different techniques. Physica D 2001;159(1-2):58–70.
[41] Shadden SC, Taylor CA. Characterization of coherent structures in the cardiovascular system. Ann Biomed Eng 2008;36(7):1152–62.
[42] Haller G. Distinguished material surfaces and coherent structures in three-dimensional fluid flows. Physica D 2001;149(4):248–77.
[43] Doorly DJ, Sherwin SJ, Franke PT, Peirò J. Vortical flow structure identification and flow transport in arteries. Comput Meth Biomech Biomed Eng 2002;5(3):261–75.
[44] Ottino JM. The kinematics of mixing: stretching, chaos and transport. Cambridge University Press 1989.
[45] Kipfer P, Reck F, Greiner G. Local exact particle tracing on unstructured grids. Comput Graph Forum 2003;22(2):133–42.
[46] Scheuermann G, Bobach T, Hagen H, Mahrous K, Hamann B, Joy KI, Kollmann W. A tetrahedra-based stream surface algorithm. In: IEEE visualization 2011, October 21–26, San Diego, USA; 2001.
[47] Chong MS, Perry AE, Cantwell BJ. A general classification of three-dimensional flow fields. Phys Fluids A 1990;2(5):765–77.
[48] da Silva CB, Pereira JCF. Invariants of the velocity-gradient, rate-of-strain, and rate-of-rotation tensors across the turbulent/nonturbulent interface in jets. Phys Fluids 2008;20(5):055101.
[49] Zabusky NJ, Boratav ON, Pelz RB, Gao M, Silver D, Cooper SP. Emergence of coherent patterns of vortex stretching during reconnection: a scattering paradigm. Phys Rev Lett 1991;67(18):2469–73.
[50] Sujudi D, Haimes R. Identification of swirling flow in 3-D vector fields. AIAA paper 95-1715; 1995.
[51] Haimes R, Kenwright D. On the velocity gradient tensor and fluid feature extraction. In: 14th AIAA computational fluid dynamics conference. AIAA paper 99-3288; 1999.
[52] Roth M, Peikert R. A higher-order method for finding vortex core lines. In: Visualization '98. Proceedings; 1998. p. 143–50.
[53] Goubergrits L, Thamsen B, Berthe A, Poethke J, Kertzscher U, Affeld K, et al. In vitro study of near-wall flow in a cerebral aneurysm model with and without coils. Am J Neuroradiol 2010;31:1521–8.
[54] Dallmann U. Topological structures of three-dimensional flow separation. DFVLR report IB 221-82-A07, Göttingen, West Germany; 1986.
[55] Oswatitsh K. Die Ablösungsbedingung von Grenzschichten. In: Goertler H, editor. Grenzschichtforschung. Springer-Verlag; 1958. p. 357–67.
[56] Hornung HG, Perry AE. Some aspects of three-dimensional separation. Part I. Streamsurface bifurcations. Z Flugwiss Weltraumforsch 1984;8:77–87.
[57] Tobak M, Peake DJ. Topology of three-dimensional separated flows. Ann Rev Fluid Mech 1982;14:61–85.
[58] Lighthill MJ. Attachment and separation in three-dimensional flow. In: Rosenhead L, editor. Laminar boundary layers. Oxford: Oxford Univ. Press; 1963. p. 72–82.
[59] Hahn C, Schwartz MA. The role of cellular adaptation to mechanical forces in atherosclerosis. Arterioscl Thromb Vasc Biol 2008;28:2101–7.
[60] Langille BL, O'Donnell F. Reductions in arterial diameter produced by chronic decreases in blood flow are endothelium-dependent. Sci New Ser 1986;231(4736):405–7.